BATTERIES & SUPERCAPS

Communications

VIP *Very Important Paper*

Integrating Fast Potential-Fringe Battery Reactions for High-Voltage Battery-Supercapacitor Hybrid Energy Storage Systems

Ziwei Xiao,[a] Shengping Wang,[a] Xiaojun Yan,[a] Congcong Liu,[a] Xiaoli Zhao,*[a] and Xiaowei Yang*[a]

The emerging of aqueous battery-supercapacitor hybrid systems (BSH) promises the combination of the excellent rate performance of supercapacitors and the capacity superiority of batteries. However, the energy density of such systems is still limited by an unsatisfying electrochemical window and the absence of voltage plateaux. To address this point, we herein propose a "potential fringe" strategy, which features a kinetically widened stable potential window and a high voltage plateau. Under this strategy, we remarkably promote the energy density of BSH by utilizing two fast battery reactions at the potential nearly below the hydrogen evolution reaction in the anode and the potential nearly above the oxygen evolution reaction in the cathode: reduced graphene oxide (rGO) hydrogel films act as the cathode and $TiO_2@rGO$ hydrogel films act as the anode with $LiOH/K_4Fe(CN)_6$ as the electrolytes. Through coupling the two fast potential-fringe reactions – a metal cation insertion/extraction in the TiO_2 electrode and a reversible redox reaction of $[Fe(CN)_6]^{4-}/[Fe(CN)_6]^{3-}$ in the cathode, the alkaline BSH reaches a high voltage of 2 V with a discharge voltage plateau of 1.55 V. Compared with the 6.2 Wh kg^{-1} and 20.3 Wh kg^{-1} for the rGO//rGO system at 1.2 V and $TiO_2@rGO$//rGO system at 1.7 V in LiOH/KOH electrolyte, the system delivers a high energy density of 70.4 Wh kg^{-1} at a power density of 2.90 kW kg^{-1}.

1. Introduction

With the fast update on electronics and the increasing demand for clean energy resources, it is crucial nowadays to pursue the goal of high-performance electrochemical energy storage systems with high energy/power densities, long service life, high safety and economic efficiency. Aqueous electrochemical energy storage, including aqueous rechargeable batteries and supercapacitors, have received intensive attention for their merits of high ionic conductivity, low cost and non-flammability.[1] Among them, aqueous supercapacitors are one of the most promising candidates due to the high power density, fast charging/discharging ability and long cycling

stability.[2] However, the low energy density of aqueous supercapacitors as the result of the limited capacities of electrode materials and narrow voltage windows due to hydrogen evolution reactions (HER) and oxygen evolution reactions (OER) in aqueous electrolytes limits their large-scale practical applications. Battery-supercapacitor hybrid systems (BSHs), which consist of a battery-type electrode with high capacity and a high-rate performance supercapacitor-type electrode, promise for efficient energy storage with combined advantages.[3] Aqueous BSHs have also made remarkable progresses in the past two decades.[3a,4] A further boost of the energy density of BSHs lies in a widened stable potential window and an enhanced capacity at the high voltage.

Much efforts have been paid to increasing the voltage of aqueous energy storage devices for a higher energy density.[1a,5] Benefiting from fast-kinetics faradic reactions, the pseudocapacitive electrode with redox reactions locating near the decomposition potential of electrolyte is a newly emerging approach to increase the voltage.[6] To our best knowledge, there are many redox reactions from advanced battery electrodes and redox electrolytes that show pseudocapacitive-like reaction kinetics and become good choice for BSHs.[7] On the other hand, due to the capacitive behavior of one electrode, the energy density of BSHs still falls below the battery counterpart. Inspired from the voltage plateau design of batteries, according to $E = \int UdQ$, where E is the energy density, U and Q are the voltage and the capacity, the charge storage capability at high voltage is important for boosting the energy density. It means that the reactions with redox peaks at the edges of the potential window should make the best contribution to the energy density.

Based on the above consideration, herein, we propose a "potential fringe" strategy to improve the energy density of BSHs which features both a kinetically widened stable potential window and a high voltage plateau. An alkaline BSH was constructed with the reduced graphene oxide (rGO) hydrogel film as the cathode and the $TiO_2@rGO$ hydrogel film as the anode in $LiOH/K_4Fe(CN)_6$ electrolyte, as shown in Figure 1. In the anode, cation insertion/extraction reaction of TiO_2 provides a potential plateau nearly below the onset potential of HER; in the cathode, the rGO-based hydrogel with high accessible surface well cooperates with the redox electrolyte $K_4Fe(CN)_6$ and provides a potential plateau nearly above the onset potential of OER. The special locations of the two battery-type reactions kinetically suppress the water decomposition indicated by an acceptable Coulombic efficiency, and meanwhile

[a] Z. Xiao, S. Wang, X. Yan, C. Liu, Dr. X. Zhao, Prof. X. Yang
School of Materials Science and Engineering
Tongji University, Shanghai 201804, China
E-mail: yangxw@tongji.edu.cn
zxl36@tongji.edu.cn
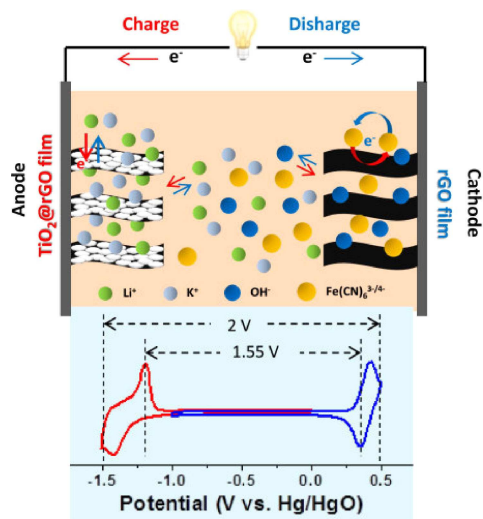Supporting information for this article is available on the WWW under
https://doi.org/10.1002/batt.201900070

Figure 1. High-voltage alkaline BSH with TiO$_2$@rGO film as the anode and rGO film as the cathode in LiOH/K$_4$Fe(CN)$_6$ electrolyte.

contribute to a high energy density. A 2 V alkaline BSH with the voltage plateau of 1.55 V and a high energy density of 70.4 Wh kg^{-1} at a high power density of 2.9 kW kg^{-1} was finally attained.

2. Results and Discussion

Porous carbon materials are the most commonly used electrode materials for supercapacitors because of their high specific surface area, good stability and abundant sources.[8] However, the HER and irreversible oxidation in aqueous electrolyte greatly limit the voltage.[5b] In this work, free-standing rGO hydrogel films were used as electrodes at first (see the illustration of preparation in Figure S1). The scanning electron microscopy (SEM) image of the cross section of rGO film is shown in Figure 2a, displaying the layered structure. The typical CV curves of rGO film in LiOH/KOH are shown in Figure 2b. The porous, connective and conductive architecture exhibits good capacitive behavior by ion adsorption/desorption. However, the irreversible currents including HER current and oxidation current emerge when the potential gradually decreases over -1 V (vs. Hg/HgO) and increases over 0.2 V vs. Hg/HgO, respectively, which cause a relatively low stable potential window, similar to the results from previous reports based on porous carbon electrodes in aqueous electrolyte.[9]

Then a higher voltage and better charge storage in the potential fringe were explored with the introduction of fast potential-fringe battery reactions. As the common battery-type electrode, titanium-based oxides are the attractive candidates for BSHs because of the advantages like good electrochemical performance, environmental benignity, low cost, high chemical
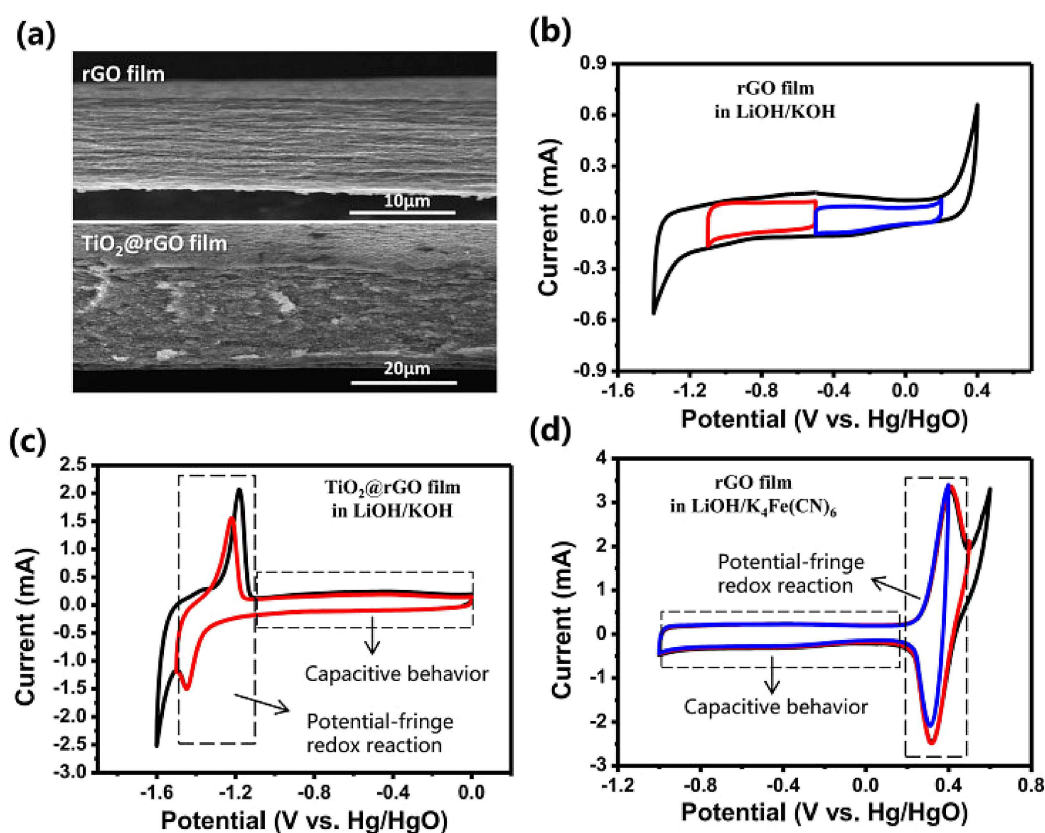

Figure 2. a) SEM images of the cross section for rGO film and TiO$_2$@rGO film, respectively. CV curves at 5 mV s^{-1} of b) rGO films in LiOH/KOH electrolyte, c) TiO$_2$@rGO films in LiOH/KOH electrolyte and d) rGO films in LiOH/K$_4$Fe(CN)$_6$ electrolyte.

and thermal stability.[10] For the anode, TiO_2 hybrid hydrogel films denoted as $TiO_2@rGO$ films were prepared through introducing TiO_2 nanoparticles into rGO hydrogel film framework according to the previous reports[11] (see Figure S1 for the schematic diagram of preparation and Figure S2 for detailed characterizations). The SEM image of $TiO_2@rGO$ film in Figure 2a indicates the structure of the freestanding films. Typical CV curves with obvious redox peaks of $TiO_2@rGO$ film electrodes in the alkaline electrolyte are shown in Figure 2c. With the potential decreasing, it exhibits capacitive behavior at first and then a pair of well-defined redox peaks at the potential fringe (when lower than −1 V vs. Hg/HgO). They correspond to the electric double layer adsorption/desorption due to the porous structure and the cation insertion/extraction reaction due to TiO_2, respectively. It should be noted that the redox reaction of TiO_2 materials occurs just at the potential nearly below HER if under alkaline condition.[12] Thus, TiO_2 occupies the redox reaction at potential fringe as in the case of Fe_2O_3[13] and succeeds in shifting the potential limitation to a lower value of −1.5 V vs. Hg/HgO.

To achieve a higher voltage and voltage plateau for the BSH, the potential and charge storage ability of the capacitive electrode should be optimized in the cathode.[10a] A fast, reversible and potential-fringe redox reaction was utilized by introducing one-electron redox couples - $[Fe(CN)_6]^{3-}/[Fe(CN)_6]^{4-}$ into the electrolyte, which has been proved to feature fast kinetics and widely used in alkaline organic flow batteries for a higher voltage[14] and supercapacitors for a higher capacity.[15] The CV curves with different potential ranges of rGO films in $[Fe(CN)_6]^{3-}/[Fe(CN)_6]^{4-}$-containing alkaline electrolyte are shown in Figure 2c. With the potential increasing, it exhibits capacitive behavior at first and then a pair of redox peaks in the range of 0.2~0.5 V (vs. Hg/HgO) emerges whose intensity can be easily regulated by adjusting the concentration of the redox electrolyte (Figure S3). Benefiting from the fast faradic reaction, it pins the upper potential limitation to 0.5 V (vs. Hg/HgO), which is comparable to that of IO_x^-/I^- redox-active electrolyte[16] and nickel/cobalt-based cathode materials.[17] Importantly, the faradic reaction just occurs near the upper potential limitation, making it feasible to match with the similar potential-fringe redox reaction of TiO_2.

2.1. The Electrochemical Performance of Cathode and Anode

The electrochemical properties of individual electrodes were investigated using a three-electrode configuration with LiOH/$K_4Fe(CN)_6$ solution as electrolyte. The CV curves of rGO films electrode at different sweep rates are displayed in Figure 3a. The redox currents are still prominent when the sweep rate reaches 50 mV s^{-1}. In addition, it exhibits good capacitive behavior due to the porous and connective structure of rGO hydrogel films when the sweep rates further increase (Figure S4). To better understand the electrochemical process, the
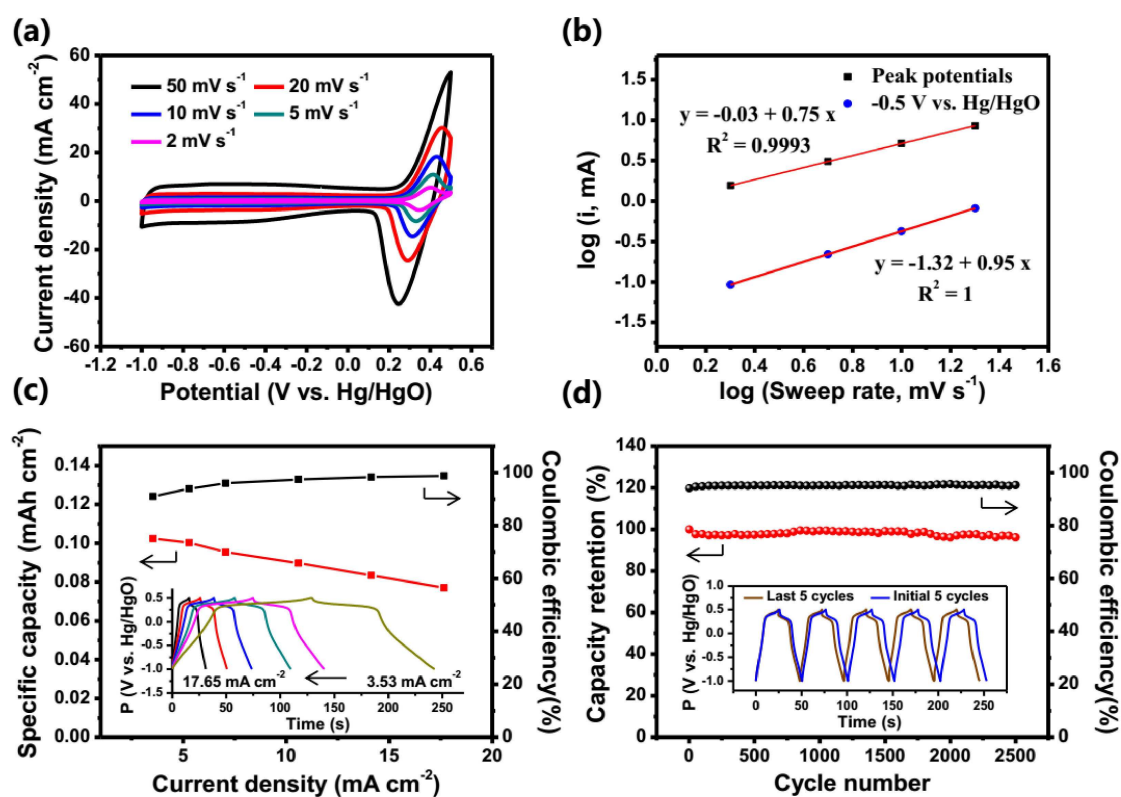

Figure 3. Electrochemical performances of rGO film electrode in LiOH/$K_4Fe(CN)_6$ electrolyte: a) CV curves at various sweep rates, b) The plots of lg i to lg v (sweep rate) for rGO film, c) Specific capacities and Coulombic efficiencies at various current densities (inset: charge/discharge curves at various current densities) and d) Cycling performance (insert: charge/discharge curves of initial 5 cycles and last 5 cycles).

power law was used to distinguish the relative contributions from the surface-controlled process and diffusion-controlled process to the total charge storage.[18] It can be expressed as follows:

$$i = a\upsilon^b$$

where i represents the current, υ is the sweep rate, and a and b are constants. The slope of the linear fit of the lg (i) versus lg (υ) at the peak potential is the b value. The b values of 0.5 and 1, represent the diffusion-controlled process and surface-controlled process, respectively. Figure 3b shows a plot of the lg (i) versus lg (υ) at of rGO film at −0.5 V (vs. Hg/HgO) and peak potentials, respectively. The b value is 0.95 at −0.5 V (vs. Hg/HgO), indicating the dominance of the surface-controlled process. And the b value is 0.75 at the redox peak potentials, indicating the redox reaction of $[Fe(CN)_6]^{4-}/[Fe(CN)_6]^{3-}$ in the cathode is controlled by both the diffusion-controlled and surface-controlled processes.

The galvanostatic discharge curves in Figure 3c clearly show the potential plateaux at the potential fringe. The specific capacity reached 0.10 mAh cm^{-2} at 3.53 mA cm^{-2} and remained 0.077 mAh cm^{-2} (77%) at 17.65 mA cm^{-2} (with an areal mass loading of 0.7 mg cm^{-2}). As shown in Figure 3d, when the cycle life are up to 2500 cycles at the charging/discharging current density of 14.13 mA cm^{-2}, the capacity can still remain 94% with a Coulombic efficiency up to 95%. These results demon-

strate that the fast potential-fringe redox reaction of $[Fe(CN)_6]^{3-}/[Fe(CN)_6]^{4-}$ can greatly improve the upper potential and capacity of the cathode.

The electrochemical properties of the anode material, TiO$_2$@rGO films electrode, were measured with LiOH/K$_4$Fe(CN)$_6$ as the electrolyte between −1.5 V and 0 V (vs. Hg/HgO). Certainly, the effect of the redox-active additive-$[Fe(CN)_6]^{3-}/[Fe(CN)_6]^{4-}$ on TiO$_2$@rGO film electrode should be considered at first. The electrochemical performance with/without redox-active additive is shown in Figure S5. Compared with LiOH/KOH electrolyte, there is no significant difference in the CV curves and capacity values between with/without redox-active additive, which suggests that the redox additive has neglectable influence on the anode. Figure 4a shows the CV curves of TiO$_2$@rGO film electrode at various sweep rates between 2 to 50 mV s^{-1}. The increased redox currents are clearly observed at higher sweep rates. In addition, it remains good capacitive behavior due to the rGO framework even when the sweep rate reaches 500 mV s^{-1} (Figure S6). Figure 4b shows the plots of the lg (i) versus lg (υ) of TiO$_2$@rGO film at the redox-peak potentials and −0.5 V (vs. Hg/HgO), respectively. The calculated b value is 0.96 at −0.5 V (vs. Hg/HgO), indicating the surface-controlled capacitive behavior. And the calculated b is 0.78 at the peak potentials for the redox reaction of TiO$_2$, indicating the cooperation of diffusion-controlled process and surface-controlled process. It is probable ascribed to the fast kinetic due to
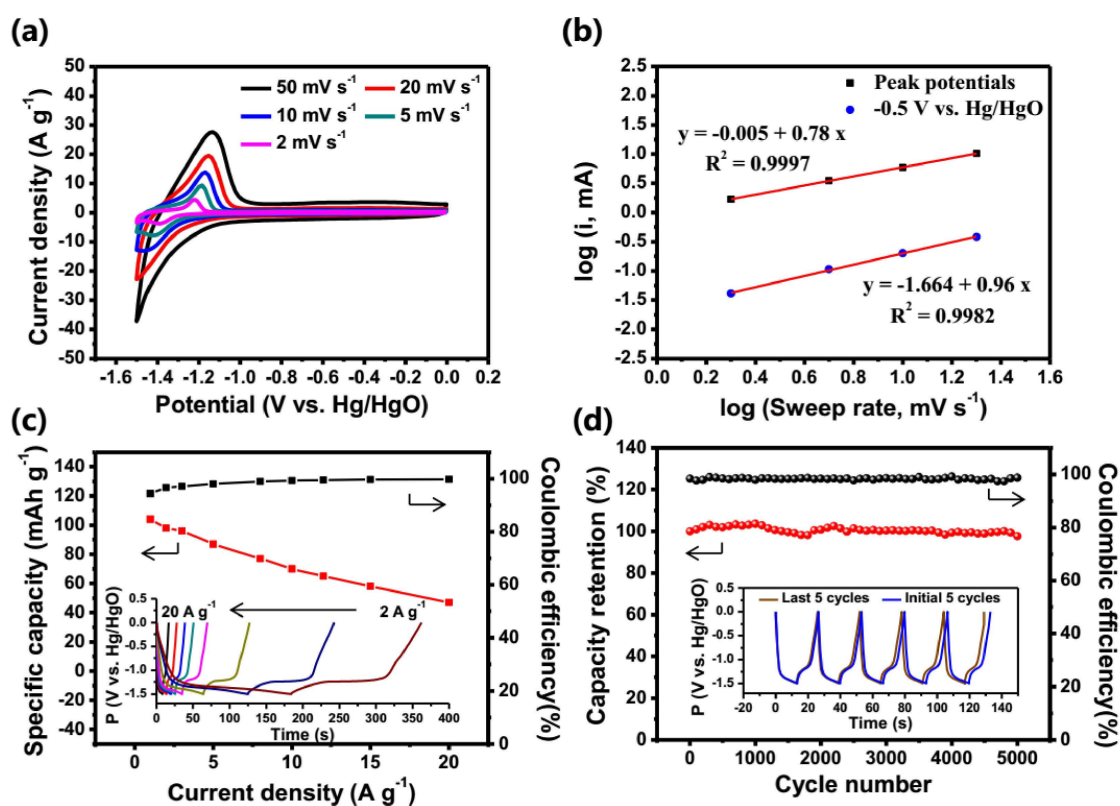

Figure 4. Electrochemical performances of TiO$_2$@rGO film electrode in LiOH/K$_4$Fe(CN)$_6$ electrolyte: a) CV curves at various sweep rates, b) The plots of lg i to lg v (sweep rate) for TiO$_2$@rGO film, and c) Specific capacities and Coulombic efficiencies at various current densities (inset: charge/discharge curves at various current densities) and d) Capacity retention and Coulombic efficiency (insert: charge/discharge curves of initial 5 cycles and last 5 cycles).

the hydrogel structure[19] and the partly pseudocapacitive contributions of TiO_2.[20]

Figure 4c shows the specific capacities according to the galvanostatic charge-discharge results. The potential plateaux in the charging process correspond to the oxidation peaks in the CV curves. It delivers the capacity values of 104, 98, 87, 70, 58 and 47 mAh g^{-1} at current densities of 1, 2, 5, 10, 15 and 20 A g^{-1} based on the mass of TiO_2@rGO film. These capacity values are much lower than the theoretical value of TiO_2 (170 mAh g^{-1}), which can be ascribed to the mass of rGO framework (20% of the total mass) and the incomplete reaction with cations in aqueous electrolyte. The cycle-life test was conducted at the charging rate of 12 A g^{-1} (Figure 4d). The capacity retention was 94% after 5000 cycles with Coulombic efficiency of 98%. The above results demonstrate the efficiency of the potential-fringe redox reaction from TiO_2 in achieving a more negative lower potential limitation and a higher capacity.

2.2. The Electrochemical Performances of the Assembled BSH

The alkaline BSH was fabricated by using TiO_2@rGO film as the anode and rGO film as the cathode with LiOH/$K_4Fe(CN)_6$ as the electrolyte. By regulating and coupling the potential-fringe redox reactions of the anode and the cathode, the capacities and potential ranges would be completely exploited. For better understanding the capacity matching, we in-situ detected the potential of the anode and cathode by introducing an additional Hg/HgO (in 1 M KOH) reference electrode in the two-electrode configuration. The loading mass of the TiO_2 and the concentration of the redox electrolyte were regulated for the redox reactions in the anode and the cathode, respectively. Different charge/discharge curves of the full cells and the corresponding potential distribution are shown in Figure S7. The full utilization of redox reactions in positive and negative electrodes was realized as shown in Figure S7a, which was selected to further test. As illustrated in Figure 5a, the charge balance should not only widen the voltage window, but also reach a higher voltage plateau for boosting the charge storage at the high voltage. CV curves of the system at various scan rates from 5 to 100 mV s^{-1} are shown in Figure 5b. Compared with the rGO//rGO system (1.2 V) and TiO_2@rGO//rGO system (1.7 V) in LiOH/KOH electrolyte (Figure S8), the maximum voltage reaches 2 V, which is higher than most of alkaline energy storage systems that previously reported.[21] Moreover, unlike the TiO_2@rGO//rGO-LiOH/KOH BSH system, it exhibits a distinguishable redox peak at high voltage of 1.55 V due to the two potential-fringe redox reactions. The voltage plateaux was further confirmed in the galvanostatic charge/discharge curves, as shown in Figure 5c. By in-situ monitoring the charge/discharge curves of individual electrodes, the potential range of the positive electrode and the negative electrode locate at 0.5~0.5 V vs. Hg/HgO and −0.5~−1.5 V vs. Hg/HgO at 5 A g^{-1}, respectively (Figure 5d). The potential range of the positive electrode becomes narrower and the negative electrode is wider when the current density increases, due to the difference in rate capacity of the cathode and the anode. As shown in

Figure 5e, the system delivers a specific capacity of 48.9 mAh g^{-1} at 2 A g^{-1} based on the total mass of rGO film and TiO_2@rGO film calculated by galvanostatic charge/discharge results, which is much higher than that of rGO//rGO (12.4 mAh g^{-1}, equivalent to 37.3 F g^{-1}) and TiO_2@rGO//rGO (24.2 mAh g^{-1}, equivalent to 51.4 F g^{-1}) in LiOH/KOH electrolyte (Figure S9). Furthermore, compared with the obvious irreversibility and lower Coulombic efficiency of rGO//rGO (LiOH/KOH) in the same voltage window (Figure S10), the assembled BHS exhibits more reasonable reversibility and higher Coulombic efficiency (90% above). These results demonstrate the voltage and the capacity of the assembled BSH are both greatly improved through coupling the two fast potential-fringe battery reactions based on TiO_2@rGO anode and rGO cathode in LiOH/$K_4Fe(CN)_6$ electrolyte.

A cycling test was carried out in the voltage window of 0~2 V at a current density of 15 A g^{-1} for 5,000 cycles. After 5,000 cycles, the capacity retention reaches 90% (Figure 6a). Furthermore, the self-discharge curve was close to that of the rGO//rGO system in alkaline electrolyte, which can be ascribed to the strong adsorption of the redox species by the rGO hydrogel (Figure S11). Figure 6b shows the comparison of the gravimetric energy and power densities of as-assembled systems. The energy densities of the BSH with redox electrolyte could reach 70.4 Wh kg^{-1} at a high power density of 2.90 kW kg^{-1} and 35.8 Wh kg^{-1} at 12.24 kW kg^{-1}, much better than the neat supercapacitor (rGO//rGO) and the BSH (TiO_2@rGO//rGO in 1 M LiOH/1 M KOH). The rGO//rGO in 1 M LiOH/1 M KOH electrolyte shows an energy density of 6.2 Wh kg^{-1} at 0.50 kW kg^{-1} and 3.5 Wh kg^{-1} at 4.76 kW kg^{-1}; TiO_2@rGO//rGO in 1 M LiOH/1 M KOH shows an energy density of 20.3 Wh kg^{-1} at 0.84 kW kg^{-1} and 9.9 Wh kg^{-1} at 6.67 kW kg^{-1}.

3. Conclusions

In summary, we propose a "potential fringe" strategy to improve the energy density of BSH which feature both a kinetically widened stable voltage window and a high voltage plateau, exampled by a novel alkaline BSH of TiO_2@rGO hydrogel films as the anode and rGO hydrogel films as the cathode with LiOH/$K_4Fe(CN)_6$ as the electrolyte. Through coupling the potential-fringe redox reactions of the cation insertion/extraction of TiO_2 in the anode and $[Fe(CN)_6]^{3-}$/$[Fe(CN)_6]^{4-}$ in the cathode, a 2 V alkaline BSH with a voltage plateau of 1.55 V is achieved. It delivers a high energy density of 70.4 Wh kg^{-1} at the high power density of 2.90 kW kg^{-1}.

Experimental Section

Preparation of Materials

Preparation of rGO Dispersion

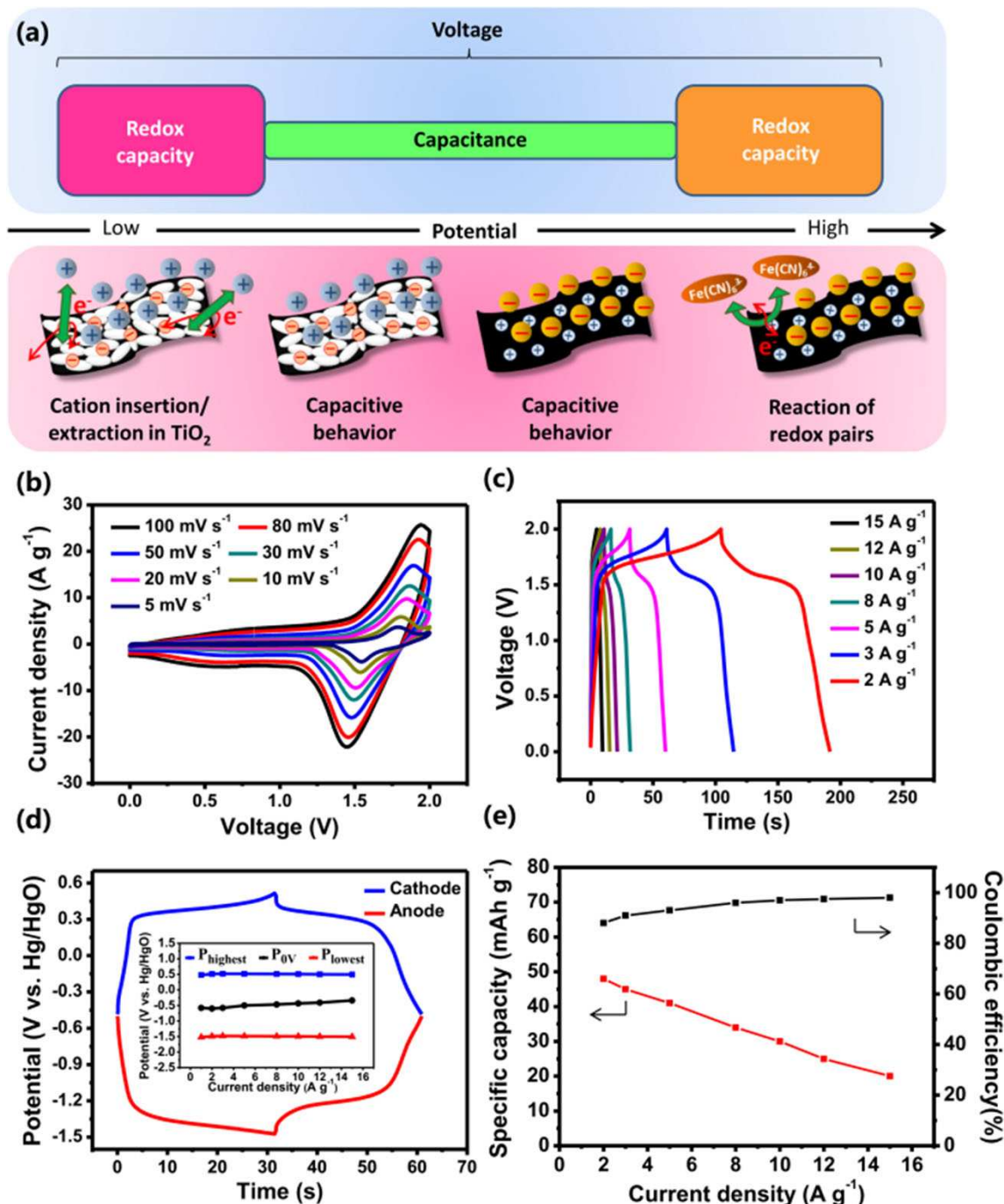Firstly, graphene oxide dispersion was prepared by modified Hummers' method. Then GO was converted to rGO according to

Figure 5. Electrochemical performances of the alkaline BSH based on TiO_2@rGO film anode and rGO film cathode in $LiOH/K_4Fe(CN)_6$ electrolyte: a) coupling of the two fast potential-fringe redox reaction; b) CV curves at various sweep rates. c) Galvanostatic charge/discharge curves. d) In-situ detection of the galvanostatic charge/discharge curves of individual electrode at 5 A g^{-1} (potential ranges at various current densities of individual electrodes in two-electrode configuration). e) The specific capacity and Coulombic efficiency in different current densities.

the previous report.[22] Briefly, GO dispersion (0.5 mg mL^{-1}) was added into a 100 mL Teflon-lined stainless autoclave. Then 0.16 mL of hydrazine hydrate (24 wt%, Alfa Aesar) and 0.56 mL of aqueous ammonia (28 wt%, Sigma-Aldrich) were added into the dispersion. The autoclave was put in the oven under 120 °C for 3 h to obtain stable rGO dispersion.

Preparation of TiO₂ Dispersion

The synthesis of TiO_2 was based on the previous reports.[11,23] Typically, 1 mL of $TiCl_4$ (Alfa Aesar) was slowly injected into the argon protected round bottomed flask followed by the addition 80 mL of ethylene glycol under magnetic stirring. After stirring for 2 h at room temperature, 2.5 mL of aqueous ammonia (28 wt%) was added for adjusting the pH to about 7 and vigorously stirring for 15 min. The solution was then transferred into a 100 mL Teflon-lined stainless autoclave and kept under 150 °C for 24 h. The
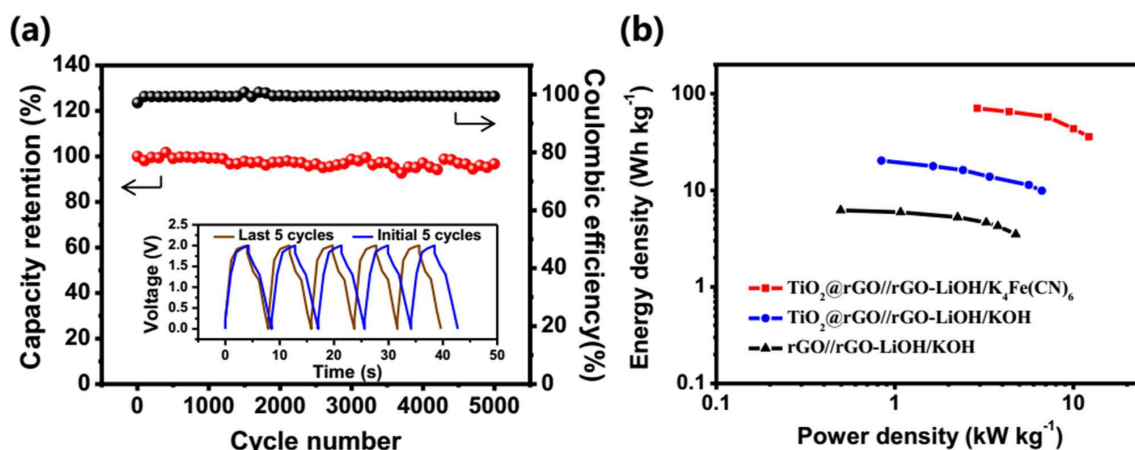
Figure 6. a) Cycle performance TiO$_2$@rGO with LiOH/K$_4$Fe(CN)$_6$ as the electrolyte. The cycling was carried out at 15 A g^{-1} (insert: charge/discharge curves of initial 5 cycles and last 5 cycles). b) Ragone plots of the alkaline BSH and the normal supercapacitor.

reaction product was centrifugally washed with ethanol and deionized water. The synthesized TiO$_2$ was then dispersed in water for further usage.

Assembly of Freestanding Hydrogel Film Electrodes

Assembly of the rGO Film Electrode

The rGO film electrode was obtained by vacuum filtration of the rGO dispersion with a mixed cellulose ester microporous filter film. Then it was peeled off from the filter film carefully and cut into 8 mm in diameter for the electrode.

Assembly of the TiO$_2$@rGO Film Electrode

The as-obtained rGO dispersion and as-synthesized TiO$_2$ dispersion were mixed uniformly. The mixed dispersion was then vacuum filtrated for TiO$_2$@GO film. The mass loading and weight ratio of TiO$_2$ and rGO could be controlled by the amount of dispersion easily. Then the hydrogel films were transferred to the 100 mL Teflon-lined autoclave for 4 h of hydrothermal reaction under 150° C. After cooling, the TiO$_2$@rGO hydrogel films were cut into 6 mm in diameter and used as the electrode directly.

Characterization

The morphology and element composition of the samples were investigated using JEM-2100 scanning electron microscopy (SEM, Hitachi S4800) and energy-dispersive X-ray spectroscopy (EDX). X-ray diffraction (XRD) profiles of the samples were obtained on D8-advance equipped with Cu Kα radiation. X-ray photoelectron spectrum (XPS) was obtained on ThermoScientific ESCALAB 250Xi spectrometer with a Al Kα source.

Electrochemical Measurements

For both three-electrode and two-electrode systems, the electrochemical measurements including cyclic voltammetry curves, galvanostatic charge/discharge curves and electrochemical impedance spectroscopy were carried out in 3-electrode Swagelok cell on a Bio-Logic VMP3 electrochemical workstation. 500 μL electrolyte was added into the cell with filter paper as the seperator. The three-electrode system was adopted for the evaluation of the

electrochemical performance of individual electrodes with glassy carbon electrode as the current collector, graphite electrode as the counter electrode and Hg/HgO in 1 M KOH as the reference electrode. For two-electrode system, the glassy carbon electrodes were used as the current collectors in both the anode and the cathode. An additional Hg/HgO in 1 M KOH reference electrode was added to in-situ detect the potential of the anode and cathode. The specific capacity in three-electrode system was calculated based on the mass of the electrode materials, and in two electrode the total mass of the cathode and anode (see Supplementary Information for detail calculation of electrochemical performance).

Conflict of Interest

The authors declare no conflict of interest.

[1] a) M. Yu, Y. Lu, H. Zheng, X. Lu, *Chem. Eur. J.* **2018**, *24*, 3639–3649; b) H. Kim, J. Hong, K. Y. Park, H. Kim, S. W. Kim, K. Kang, *Chem. Rev.* **2014**, *114*, 11788–11827.

[2] G. Wang, L. Zhang, J. Zhang, *Chem. Soc. Rev.* **2012**, *41*, 797–828.

[3] a) W. Zuo, R. Li, C. Zhou, Y. Li, J. Xia, J. Liu, *Adv. Sci.* **2017**, *4*, 1600539; b) N. Choudhary, C. Li, J. Moore, N. Nagaiah, L. Zhai, Y. Jung, J. Thomas, *Adv. Mater.* **2017**, *29*, 1605336; c) B. Zhao, L. Zhang, Q. Zhang, D. Chen, Y. Cheng, X. Deng, Y. Chen, R. Murphy, X. Xiong, B. Song, C. Wong, M. Wang, M. Liu, *Adv. Energy Mater.* **2018**, *8*, 1702247; d) M. Huang, M. Li, C. Niu, Q. Li, L. Mai, *Adv. Funct. Mater.* **2019**, 1807847.

[4] a) R. Li, Y. Wang, C. Zhou, C. Wang, X. Ba, Y. Li, X. Huang, J. Liu, *Adv. Funct. Mater.* **2015**, *25*, 5384–5394; b) Z. Zhai, K. Huang, X. Wu, *Nano Energy* **2018**, *47*, 89–95; c) Y. Jiao, J. Pei, C. Yan, D. Chen, Y. Hu, G. Chen,

J. Mater. Chem. A **2016**, *4*, 13344–13351; d) R. Wang, J. Lang, P. Zhang, Z. Lin, X. Yan, *Adv. Funct. Mater.* **2015**, *25*, 2270–2278.

[5] a) X. Zang, C. Shen, M. Sanghadasa, L. Lin, *ChemElectroChem* **2018**, *6*, 976–988; b) C. Liu, Y. Liu, T. Yi, C. Hu, *Carbon* **2019**, *145*, 529–548; c) L. Suo, O. Borodin, T. Gao, M. Olguin, J. Ho, X. Fan, C. Luo, C. Wang, K. Xu, *Science* **2015**, *350*, 938–943; d) D. Xiao, Q. Wu, X. Liu, Q. Dou, L. Liu, B. Yang, H. Yu, *ChemElectroChem* **2018**, *6*, 439–443; e) S. Wang, X. Zhao, X. Yan, Z. Xiao, C. Liu, Y. Zhang, X. Yang, *Angew. Chem. Int. Ed.* **2019**, *58*, 205–210.

[6] a) N. Jabeen, A. Hussain, Q. Xia, S. Sun, J. Zhu, H. Xia, *Adv. Mater.* **2017**, *29*, 1700804; b) R. Sahoo, D. T. Pham, T. H. Lee, T. Luu, J. Seok, Y. H. Lee, *ACS Nano* **2018**, *12*, 8494–8505; c) T. Xiong, T. Tan, L. Lu, W. S. V. Lee, J. Xue, *Adv. Energy Mater.* **2018**, *8*, 1702630.

[7] a) S. Zhang, B. Yin, X. Liu, D. Gu, H. Gong, Z. Wang, *Nano Energy* **2019**, *59*, 41–49; b) V. Augustyn, J. Come, M. A. Lowe, J. W. Kim, P. L. Taberna, S. H. Tolbert, H. D. Abruna, P. Simon, B. Dunn, *Nat. Mater.* **2013**, *12*, 518–522; c) K. A. Owusu, L. Qu, J. Li, Z. Wang, K. Zhao, C. Yang, K. M. Hercule, C. Lin, C. Shi, Q. Wei, L. Zhou, L. Mai, *Nat. Commun.* **2017**, *8*, 14264; d) S. E. Chun, B. Evanko, X. Wang, D. Vonlanthen, X. Ji, G. D. Stucky, S. W. Boettcher, *Nat. Commun.* **2015**, *6*, 7818; e) T. Wang, H. C. Chen, F. Yu, X. S. Zhao, H. Wang, *Energy Storage Mater.* **2019**, *16*, 545–573; f) P. Wang, R. Wang, J. Lang, X. Zhang, Z. Chen, X. Yan, *J. Mater. Chem. A* **2016**, *4*, 9760–9766.

[8] A. Ghosh, Y. H. Lee, *ChemSusChem* **2012**, *5*, 480–499.

[9] a) M. Alhabeb, M. Beidaghi, K. L. Van Aken, B. Dyatkin, Y. Gogotsi, *Carbon* **2017**, *118*, 642–649; b) K. Yuan, Y. Xu, J. Uihlein, G. Brunklaus, L. Shi, R. Heiderhoff, M. Que, M. Forster, T. Chasse, T. Pichler, T. Riedl, Y. Chen, U. Scherf, *Adv. Mater.* **2015**, *27*, 6714–6721.

[10] a) X. Yan, X. Zhao, C. Liu, S. Wang, Y. Zhang, M. Guo, Y. Wang, L. Dai, X. Yang, *J. Power Sources* **2019**, *423*, 331–338; b) L. Ye, Q. Liang, Y. Lei, X. Yu, C. Han, W. Shen, Z. Huang, F. Kang, Q. Yang, *J. Power Sources* **2015**, *282*, 174–178; c) C. Jiang, J. Zhao, H. Wu, Z. Zou, R. Huang, *J. Power Sources* **2018**, *401*, 135–141.

[11] a) X. Yan, Y. Wang, C. Liu, M. Guo, J. Tao, J. Cao, D. Fu, L. Dai, X. Yang, *J. Energy Chem.* **2018**, *27*, 176–182.

[12] a) M. Manickam, P. Singh, T. B. Issa, S. Thurgate, *J. Appl. Electrochem.* **2006**, *36*, 599–602; b) S. Liu, G. Pan, N. Yan, X. Gao, *Energy Environ. Sci.* **2010**, *3*, 1732–1735; c) J. Liu, J. Wang, Z. Ku, H. Wang, S. Chen, L. Zhang, J. Lin, Z. Shen, *ACS Nano* **2016**, *10*, 1007–1016; d) Y. Yu, D. Sun, H. Wang, H. Wang, *Nanoscale Res. Lett.* **2016**, *11*, 448.

[13] a) H. Wang, Z. Xu, H. Yi, H. Wei, Z. Guo, X. Wang, *Nano Energy* **2014**, *7*, 86–96; b) B. Liu, M. Zhao, L. Han, X. Lang, Z. Wen, Q. Jiang, *Chem. Eng. J.* **2018**, *335*, 467–474.

[14] a) D. G. Kwabi, K. Lin, Y. Ji, E. F. Kerr, M. A. Goulet, D. De Porcellinis, D. P. Tabor, D. A. Pollack, A. Aspuru-Guzik, R. G. Gordon, M. J. Aziz, *Joule* **2018**; b) Z. Yang, L. Tong, D. P. Tabor, E. S. Beh, M. A. Goulet, D. De Porcellinis, A. Aspuru-Guzik, R. G. Gordon, M. J. Aziz, *Adv. Energy Mater.* **2018**, *8*, 1702056.

[15] a) J. Y. Hwang, M. Li, M. F. El-Kady, R. B. Kaner, *Adv. Funct. Mater.* **2017**, *27*, 1605745; b) J. Hwang, M. F. El-Kady, M. Li, C. Lin, M. Kowal, X. Han, R. B. Kaner, *Nano Today* **2017**, *15*, 15–25.

[16] X. Wang, R. S. Chandrabose, S. E. Chun, T. Zhang, B. Evanko, Z. Jian, S. W. Boettcher, G. D. Stucky, X. Ji, *ACS Appl. Mater. Interfaces* **2015**, *7*, 19978–19985.

[17] a) J. Yang, C. Yu, C. Hu, M. Wang, S. Li, H. Huang, K. Bustillo, X. Han, C. Zhao, W. Guo, Z. Zeng, H. Zheng, J. Qiu, *Adv. Funct. Mater.* **2018**, *28*, 1803272; b) J. Lin, H. Jia, H. Liang, S. Chen, Y. Cai, J. Qi, C. Qu, J. Cao, W. Fei, J. Feng, *Adv. Sci.* **2018**, *5*, 1700687.

[18] a) H. S. Kim, J. B. Cook, H. Lin, J. S. Ko, S. H. Tolbert, V. Ozolins, B. Dunn, *Nat. Mater.* **2017**, *16*, 454–460; b) V. Augustyn, P. Simon, B. Dunn, *Energy Environ. Sci.* **2014**, *7*, 1597–1641.

[19] X. Yang, J. Zhu, L. Qiu, D. Li, *Adv. Mater.* **2011**, *23*, 2833–2838.

[20] J. Wang, J. Polleux, J. Lim, B. Dunn, *J. Phys. Chem. C* **2007**, *111*, 14925–14931.

[21] a) H. Wang, Y. Song, W. Liu, L. Yan, *J. Alloys Compd.* **2018**, *735*, 2428–2435; b) M. Hwang, J. Kang, K.-d. Seong, D. K. Kim, X. Jin, W. H. Antink, C. Lee, Y. Piao, *Electrochim. Acta* **2018**, *270*, 156–164; c) H. Chen, Y. Qin, H. Cao, X. Song, C. Huang, H. Feng, X. S. Zhao, *Energy Storage Mater.* **2019**, *17*, 194–203; d) J. Yan, Z. Fan, W. Sun, G. Ning, T. Wei, Q. Zhang, R. Zhang, L. Zhi, F. Wei, *Adv. Funct. Mater.* **2012**, *22*, 2632–2641.

[22] D. Li, M. B. Muller, S. Gilje, R. B. Kaner, G. G. Wallace, *Nat. Nanotechnol.* **2008**, *3*, 101–105.

[23] S. Liu, H. Jia, L. Han, J. Wang, P. Gao, D. Xu, J. Yang, S. Che, *Adv. Mater.* **2012**, *24*, 3201–3204.